Journal of Power Sources 471 (2020) 228480

Contents lists available at ScienceDirect

Journal of Power Sources

journal homepage: www.elsevier.com/locate/jpowsour

Artificial interface stabilized $LiNi_{0.80}Co_{0.15}Al_{0.05}O_2$@Polysiloxane cathode for stable cycling lithium-ion batteries

Zi Yang [a], Zhimin Li [a,*], Yunxia Huang [a], Maolin Zhang [a], Chaofeng Liu [b], Dongyan Zhang [a], Guozhong Cao [b,**]

[a] School of Advanced Materials and Nanotechnology, Xidian University, Xi'an, 710071, PR China
[b] Department of Materials Science and Engineering, Clean Energy Institute, University of Washington, Seattle, 98195, WA, USA

HIGHLIGHTS

- A thin conformal polysiloxane is firmly wrapped on the surface of $LiNi_{0.8}Co_{0.15}Al_{0.05}O_2$.
- Polysiloxane layer reduces trace water and removes HF, while suppresses the side reaction.
- $LiNi_{0.8}Co_{0.15}Al_{0.05}O_2$@Polysiloxane delivers ultrahigh long cycling stability.

GRAPHICAL ABSTRACT

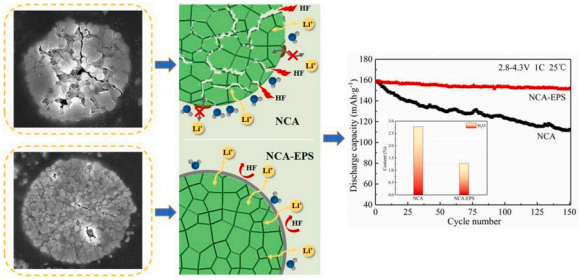

ARTICLE INFO

Keywords:
Cycling stability
Surface modification
Polysiloxane
$LiNi_{0.80}Co_{0.15}Al_{0.05}O_2$
Lithium-ion battery

ABSTRACT

$LiNi_{0.80}Co_{0.15}Al_{0.05}O_2$ (NCA) as a practical cathode material for lithium-ion batteries has been attracting extensive attention owing to its superior specific capacity and small voltage hysteresis, but suffers from the serious side reactions with electrolyte and HF erosion resulting in capacity fading. A thin conformal polysiloxane with ethoxy-functional groups (EPS) is successfully grown on NCA particles through the hydrolysis-condensation method effectively suppresses the side reactions and mitigates the instability of NCA cathode. The original discharge capacities of NCA and NCA-EPS cathodes are 158 and 159 mAh g^{-1} at 25 °C, respectively. The capacity retention of NCA-EPS cathode is ~96% of the original capacity after 150 cycles under 1 C, 25% higher than NCA cathode. Even at 55 °C, NCA-EPS cathode could maintain ~86% of the original discharge capacity through 150 cycles, which enhances 29% compared to NCA cathode. The excellent cycling stability of NCA originates from the EPS that acts as a protective shell to reduce the trace water on the NCA surface, inhibit the side reaction and remove HF from the electrolyte through a nucleophilic substitution reaction.

* Corresponding author.
** Corresponding author.
E-mail addresses: zmli@mail.xidian.edu.cn (Z. Li), gzcao@uw.edu (G. Cao).

https://doi.org/10.1016/j.jpowsour.2020.228480
Received 19 April 2020; Received in revised form 3 June 2020; Accepted 7 June 2020
Available online 29 June 2020

1. Introduction

Lithium ion batteries (LIBs) are recognized as the reliable energy storage and conversion systems for electric vehicles and portable electronics due to their high energy density and excellent cycling performance [1–4]. As one of the most important components of LIBs, cathode materials determines the operating voltage of batteries within the safe electrochemical window of the electrolyte and restrains the energy density of batteries. Layered Nickel-rich $LiNi_{0.80}Co_{0.15}Al_{0.05}O_2$ (NCA) cathode stands out among many LIBs cathode materials for its superior reversible capacity, small polarization and good thermal stability [5–8]. However, some drawbacks and challenges for NCA cathode materials still remain [9]. For example, the surface side reactions that occurs when the active electrode is in contact with electrolyte could generate the degenerative capacity. Firstly, in the discharge process, the active Ni^{3+} will inevitably be oxidized to the unstable and inactive Ni^{4+} [10,11]. Because Ni^{4+} has strong oxidation, it will accelerate the decomposition of the electrolyte and cause the surface side reactions between active material and the electrolyte to formulate the non-conductive solid electrolyte interface (SEI) film, which will influence the Li^+ transport and increase electrochemical polarization in the NCA electrode materials [12]. Next, the inevitable trace water of the cathode particles surface will react with the solute of electrolyte ($LiPF_6$), it would decomposed into the profitless products, such as HF, LiF and POF_3. The presence of HF could arouse the dissolution of transition metal ions, resulting in further deterioration of the surface structure of active NCA material [13,14]. In addition, Ni^{2+} ions derived from the conversion of Ni^{3+} or Ni^{4+} ions easily exchanges their positions with the adjacent Li^+ ions because of the close ionic radius of Ni^{2+} (69 p.m.) and Li^+ (76 p.m.) ions, which results in cation mixing to form a NiO-like passivation layer [15,16]. The passivation layer could cause a permanent loss of capacity owning to the active lithium layer destroyed in the lattice [17].

Surface modification techniques are now commonly used to improve the properties of cathode materials, coating is one of the most important methods. The coating layer covers the surface of cathode particles and can effectively isolate the electrode from the electrolyte to control the surface side reactions [18,19]. Different kinds of materials are being explored, such as metal oxides (SiO_2, TiO_2, Al_2O_3) [20–23], metal fluoride (AlF_3, FeF_3) [24–26], metal phosphates ($Ni_3(PO_4)_2$, $FePO_4$, Li_3PO_4) [27–29], mixed oxides (Li_2O–ZrO_2, Li_2O–$2B_2O_3$) [30,31], carbon materials (graphene [32], Carbon nanotubes [33]), and Poly (3, 4-ethylenedioxythiophene) (PEDOT) [34]. These coatings form a physical barrier on the active particles surface to keep the structure from being damaged and inhibit the interfacial side reaction to some extent. HF erosion of the active electrode can be eliminated and the dissolution of transition metal ions could be suppressed. But for most coatings, the harm of HF to cathode materials has not been fundamentally solved. In addition, $LiOH/LiCO_3$ and H_2O on the surface of layered NCA cathode. These harmful products will accelerate the generation of HF, resulting in irreversible attenuation of capacity [35–37]. Therefore, an ideal coating should protect the electrode from the surface side reactions, as well as eliminate trace water adsorbed on NCA and HF in electrolyte.

Tetraethyl orthosilicate (TEOS) is easily hydrolyzed to formed the polysiloxane with ethoxy-functional groups (EPS) because of the sensitivity to H_2O [38]. The polysiloxane is widely being used in the fields of binder and textile or biomedical coatings because of the good film formation, strong adhesion and high/low temperature adaptability [39,40]. In addition, ethoxy-functional groups in polysiloxane coating could eliminate the harmful HF from the electrolyte through providing reaction sites for nucleophilic substitution of Si and F [41,42]. However, it is rarely reported that the electrochemical performances were improved through covering the polysiloxane on the cathode materials in LIBs. Therefore, EPS act a coating of active materials can cut down the interface side reactions to enhance the electrochemical performance of NCA cathode through eliminating H_2O on the NCA surface and HF in the electrolyte. Water is always used as reactant for the hydrolysis of TEOS to form the coating, but it could cause an irreversible damage on NCA and the calcination would remove ethoxy-functional groups and lose the ability of HF clearance [43,44]. Therefore, it is imperative to explore a new and reliable approach to obtain polysiloxane coating with a large number of ethoxy-functional groups to improve the electrochemical performances of NCA.

Herein, we report a scheme by establishing a protective polysiloxane coating on the layered NCA cathode. EPS film was grown on the NCA particles surface by a simple interface hydrolysis-condensation technique. The EPS film could be formed through the condensation after TEOS was subjected to the hydrolysis of trace water adsorbed on NCA particles at room temperature. This method can avoid an irreversible damage on NCA material and the decrease of ethoxy-functional groups during heat treatment process. The cycling stability of NCA coated with EPS (NCA-EPS) cathode was significantly improved. The capacity retention rate of NCA with EPS are 95.7% and 85.7% at 25 °C and 55 °C under 1C after 150 cycles, respectively. By contrast, the pristine NCA only maintains 71% and 57.6%, respectively. This study suggests a simple way to mitigate the effects of interface adverse reactions, HF corrosion, and their interactions on performance degradation after long cycle of NCA.

2. Experimental section

2.1. Materials synthesis

EPS coated NCA particles was synthesized via an in-situ hydrolysis-condensation reaction. The commercially available $Ni_{0.80}Co_{0.15}Al_{0.05}(OH)_2$ precursor (Zhichuan, Haian) was mixed with $LiOH{\cdot}H_2O$ (99%, Aladdin) at a molar ratio of 1:1.07. The mixture was heat treated at 450 °C for 5 h and then calcined at 760 °C for 12 h with a heating rate of 10 °C min^{-1} under an oxygen atmosphere. Tetraethyl orthosilicate (TEOS, 99%, Aladdin) was mixed with 50 mL absolute ethyl alcohol with stirring to generate a clear solution, followed by NCA powders (n_{TEOS}: $n_{NCA} = 0.03$) was added. The above mixture was continuously stirred at 25 °C for 4 h until the ethanol was adequately evaporated and then the resultant powders was referred to as NCA-EPS. Meantime, samples with different mole ratios of TEOS to NCA (n_{TEOS}: $n_{NCA} = 0.01$ and 0.05) were also prepared at the same condition and referred to as NCA-EPS1 and NCA-EPS5, respectively.

2.2. Materials characterization

Karl Fischer Moisture Titrator (870 KF Titrino plus, Switzerland) was used to determine the water content of the surface of NCA particles. X-ray diffractometer (XRD, BRUKER D8 Advance, Germany) was employed to identify the phases of the as-prepared samples. Field emission scanning electron microscopy (FESEM, JEOL, JSM-7500F, Japan) and transmission electron microscopy (TEM, JEOL, JSM-2100F, Japan) were adopted to observe morphologies and analyze the crystal structures of the samples. The chemical valence states and compositions of the samples were analyzed by using X-ray photoelectron spectroscopy (XPS, THERMO, ESCALAB 250XI, USA). The tests were carried out with a monochromatic Al Kα (1486.6 eV) source at a voltage 15 kV and beam current 15 mA with the vacuum about 5×10^{-9} mbar. C 1s hydrocarbon peak at 284.8 eV is used to calibrate the binding energy. The thermal stabilities of the pristine and NCA-EPS electrodes under the charged state were studied by differential scanning calorimetry (DSC, NETZSCH, STA+449F5, Germany).

2.3. Electrochemical measurements

The batteries were assembled into CR2016 coin-type batteries in an argon glove box with Li wafers as the anode, Celgard 2325 as the separator and 1 mol L^{-1} $LiPF_6$ solution as the electrolyte [45,46]. The cathode was prepared by mixing the NCA or NCA-EPS samples with

Super-P carbon and polyvinylidene fluoride (PVDF) dissolved in N-methyl-2-pyrrolidone (NMP) according to the mass ratio of 8: 1: 1. And then the above mixture was ground into a uniform slurry. The slurry was painted onto an Al foil and followed by drying at 120 °C overnight.

The electrochemical performance of the CR2016 coin-type cell was characterized using cyclic voltammograms (CVs), electrochemical impedance spectroscopy (EIS) and galvanostatic charge-discharge (GCD) via an electrochemical working station (CHI660E, CHENHUA, China) and multichannel galvanostatic system (CT2001A, LANHE, China). CVs were measured at a scan rate of 0.1 mV s^{-1} within a voltage range of 2.5–4.5 V. After the cell was activated at a rate of 0.05 C at room temperature, the charge-discharge cycles were carried out at the current density of 1 C (= 180 mA g^{-1}) for 150 cycles at 25 and 55 °C, respectively. EIS was carried out in the frequency range of 0.01 Hz–100 kHz and an amplitude of 5 mV.

3. Results and discussion

The phase structures of the as-synthesized samples were identified using XRD analysis. Fig. 1a shows the XRD image of NCA and NCA-EPS powders samples. The diffraction peaks at 2θ = 18.75, 36.58, 44.38, 48.58, 58.67 and 68.05° for the NCA powders sample are correspond to (003), (101), (104), (015), (107) and (113) lattice planes of α-$NaFeO_2$-structured phase (JCPDS card No. 74–0919) [33,47]. The splitting peaks of (006)/(102) and (108)/(110) lattice planes demonstrate the ordered layered structure in NCA [48,49]. The peak intensities and positions of NCA-EPS sample change scarcely after covering EPS on the surface of NCA particles, which indicates the EPS coating does not influence the NCA crystal phase. The XRD patterns of NCA-EPS1 and NCA-EPS5 also showed the same results (Fig. S1, Supporting Information). The result could be further confirmed through the Rietveld refinement of XRD pattern. In this study, Rietveld refinement was introduced to qualitatively evaluate the variation in the lattice parameters with the structural model of $(Li_{1-z}Ni_z)^{3a}$ $[Li_zNi_{0.8-z}Co_{0.15}Al_{0.05}]^{3b}\{O_2\}^{6c}$ via GSAS/EXPGUI software [50]. Fig. 1b and c depict the Rietveld refinement results of NCA and NCA-EPS samples, respectively. The lattice constants of NCA and NCA-EPS obtained from Rietveld analysis are listed in Table 1. NCA and NCA-EPS have the approximate lattice constants, c/a values and the intensity ratio of $I_{(003)}/I_{(104)}$, which illuminates the similar layered structure and the cation mixing degree in both samples [51]. So the layer structure and the cation mixing of NCA are influenced scarcely by EPS. The XPS spectra (Fig. S2, Supporting Information) of NCA and NCA-EPS samples reveal the existence of Ni, Co, O and Al elements. However, Si element appears in the NCA-EPS sample, which could be attributed to the presence of polysiloxane with ethoxy-functional groups. Fig. 1d and e displays the high resolution spectra of Ni 2p and Co 2p of NCA and NCA-EPS, respectively. There is no obvious difference in the position and strength of binding energy in Ni 2p and Co 2p spectra of the two samples, indicating that EPS coating has no impact on the chemical state of the elements in NCA cathode materials. In Fig. 1d, Ni 2p spectra reveal primarily two spin-orbit doublets (Ni $2p_{3/2}$ and Ni $2p_{1/2}$) along with two shake-up satellites (indicated as "Sat"), which are split into four peaks through Gaussian fitting method, manifesting the presence of Ni^{2+} and Ni^{3+} cations. The main peaks at 854.3/872.7 eV and 855.8/874.1 eV are assigned to Ni^{2+} and Ni^{3+} [52–54]. The positions of the two smooth satellite peaks are respectively at 861.5 and 878.9 eV, which reveal that Ni^{3+} are the majority in samples [55]. As for the Co 2p spectra in Fig. 2e also exhibits mainly two spin-orbit doublets (Co $2p_{1/2}$ and Co $2p_{3/2}$) along with two weak shake-up satellites. The fitted peaks at 779.8 and 794.8 eV are assigned to Co^{3+} ions, at 781.3 and 796.5 eV are indexed to Co^{2+} ions [56]. Fig. 1f depicts the high-resolution XPS spectrum of Si 2p for NCA-EPS sample. The binding energy at 102.6 eV confirms the existence of Si–O bond [40]. Therefore, the successful formation of EPS coating on the NCA particle surface is shown as a result in the XPS profile.

Fig. 2a and b shows the typical FESEM images of NCA particles in the different magnification. It is found that the spherical morphology of

Table 1
Rietveld analysis results of NCA and NCA-EPS.

Sample	Lattice parameters			$I_{(003)}/I_{(104)}$	Ni in Li site	R_p (%)	R_{wp} (%)
	a (Å)	c (Å)	c/a				
NCA	2.8685	14.188	4.9461	1.2389	0.0801	3.21	5.01
NCA-EPS	2.8688	14.189	4.9459	1.2392	0.0795	3.45	5.84

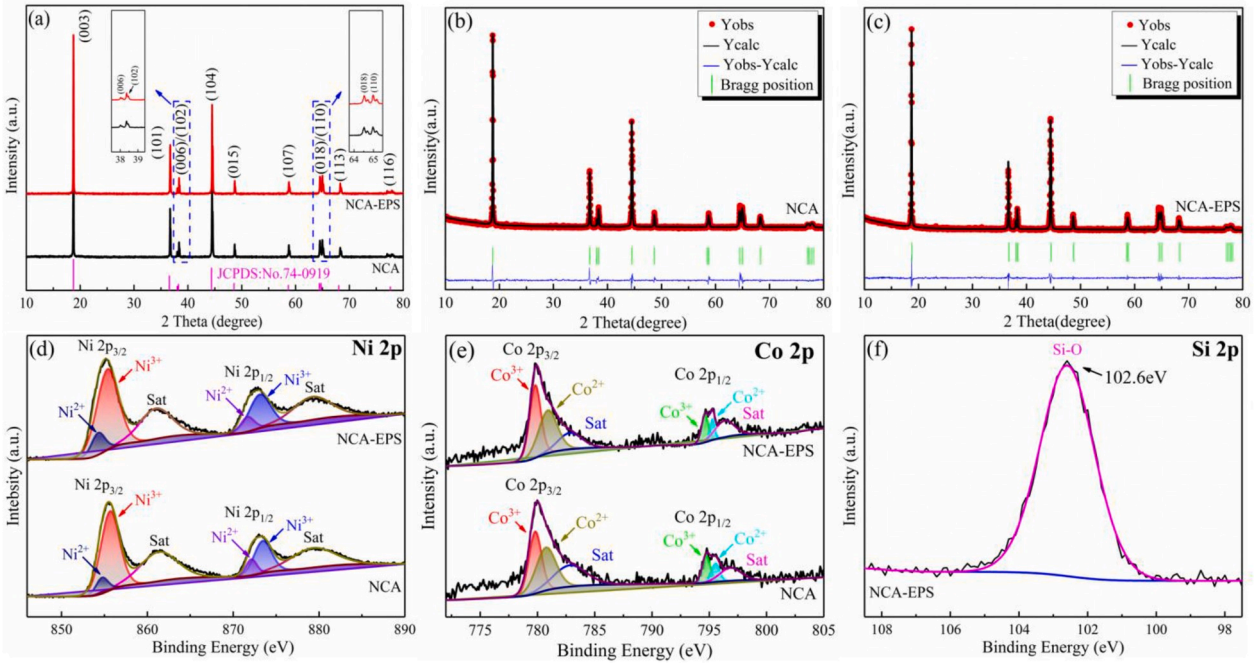

Fig. 1. (a) XRD patterns of NCA and NCA-EPS powders; (b–c) Rietveld refinement results of NCA (b) and NCA-EPS (c) samples; The high-resolution XPS spectra of (d) Ni 2p and (e) Co 2p for NCA and NCA-EPS samples and (f) the high-resolution XPS spectrum of Si 2p for NCA-EPS sample.

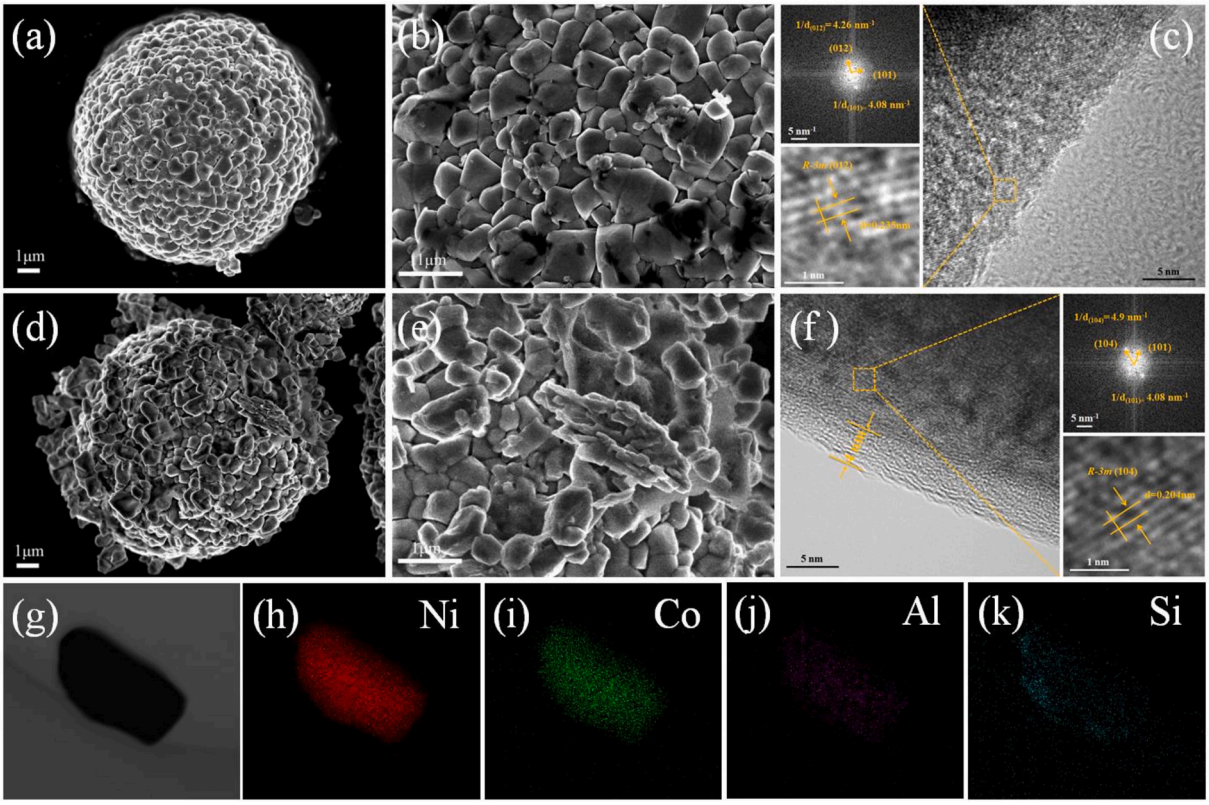

Fig. 2. The typical FESEM images of NCA and NCA-EPS samples: (a) the particles of NCA at low magnification; (b) the NCA particles at high magnification; (c) HRTEM images of NCA particle, the inset is the FFT diffraction patterns and lattice fringes; (d) the particles of NCA-EPS at low magnification; (e) the NCA-EPS particles at high magnification; (f) HRTEM images of NCA-EPS particle, the inset is the FFT diffraction patterns and lattice fringes; EDS elemental mapping images of NCA-EPS particle: (g) NCA-EPS particle, (h) Ni, (i) Co, (j) Al, (k) Si.

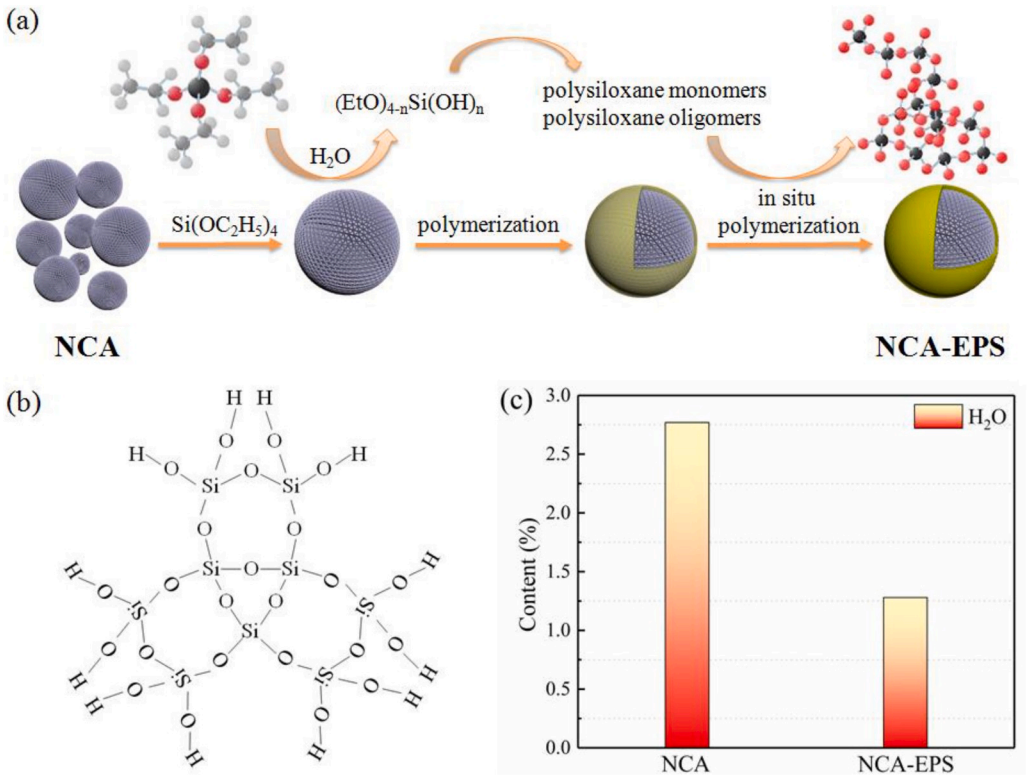

Fig. 3. (a) Schematic illustration of NCA-EPS through an in-situ hydrolysis-condensation reaction; (b) The molecular structure of polysiloxane; (c) The content of water on NCA and NCA-EPS particles surface.

NCA particles at low magnification from Fig. 2a is consisted of the aggregates of inhomogeneous microparticles at high magnification from Fig. 2b. The FESEM photos of NCA-EPS particles in the different magnification are shown in Fig. 2d and e. Compared with NCA particles, NCA-EPS particles also exhibit the spherical morphology composed of the aggregates of inhomogeneous microparticles. In addition, NCA-EPS particles display the rougher surface which may be derived from the presence of EPS coating from Fig. 2e. NCA-EPS1 and NCA-EPS5 samples also display the similar morphologies and various surface roughness compared with NCA sample (Fig. S3, Supporting Information). Fig. 2c and f are the representative HRTEM images of NCA and NCA-EPS samples, respectively, the insets in Fig. 2c and f are the corresponding fast Fourier transformation (FFT) diffraction patterns and lattice fringes. From the insets, the both samples present the excellent crystallinity. The clear lattice fringes with the interplanar spacings of 0.235 nm (Figs. 2c) and 0.204 nm (Fig. 2f) which are assigned to the (012) and (104) planes of NCA crystal, respectively. Further, a distinct coating layer with about 4 nm thickness is observed on the NCA-EPS particles surface in Fig. 2f. To confirm the ingredient of the coating, EDS element mapping of NCA-EPS particle is shown Fig. 2g and k. The result reveals Si element appears on the NCA-EPS particle in addition to Ni, Co and Al elements, showing that the EPS coating was evenly coated on the NCA particles surface through the hydrolysis-condensation method.

Fig. 3a depicts the schematic illustrating of the reducing trace water on the NCA surface through the formation of EPS coating by an in-situ hydrolysis-condensation reaction. First, TEOS is hydrolyzed by the trace water on the surface of NCA particles to generate $(EtO)_{4-n}Si(OH)_n$. And then $(EtO)_{4-n}Si(OH)_n$ could generate self-polymerize to form the dipolymer $(EtO)_{4-n}$ $(OH)_{n-1}Si–O–Si(OH)_{n-1}$ $(EtO)_{4-n}$. Also, $(EtO)_{4-n}Si(OH)_n$ could produce copolymerization with TEOS to form the dipolymer $(EtO)_{4-n}$ $(OH)_{n-1}Si–O–Si(OEt)_{n-1}$ $(EtO)_{4-n}$. Furthermore, the dipolymer $(EtO)_{4-n}$ $(OH)_{n-1}Si–O–Si(OH)_{n-1}$ $(EtO)_{4-n}$ and $(EtO)_{4-n}$ $(OH)_{n-1}Si–O–Si(OEt)_{n-1}$ $(EtO)_{4-n}$ can be polymerized continually in situ to form EPS coating with three-dimensional network structure. The process could be represented by the following equations [38–40]:

$$Si(OEt)_4 + nH_2O \rightarrow (EtO)_{4-n}Si(OH)_n + nEtOH (n = 1, 2, 3, 4) \quad (1)$$

$$(EtO)_{4-n}Si(OH)_n + (EtO)_{4-n}Si(OH)_n \rightarrow (EtO)_{4-n}(HO)_{n-1}Si - O - Si(OH)_{n-1}(EtO)_{4-n} + H_2O \quad (2)$$

$$(EtO)_{4-n}Si(OH)_n + Si(OEt)_4 \rightarrow (EtO)_{4-n}(HO)_{n-1}Si - O - Si(OEt)_{n-1}(EtO)_{4-n} + EtOH \quad (3)$$

$$m(\equiv Si - O - Si \equiv) \rightarrow \left[\begin{array}{c} \vdots \\ -O- Si - \\ \vdots \end{array} \right]_m \quad (4)$$

The molecular structure of EPS is displayed in Fig. 3b. The formation of EPS coating because of the TEOS hydrolysis could also be verified through the distinct decreased content of water absorbed on NCA-EPS particles surface. Fig. 3c depicts the content of trace water on NCA and NCA-EPS particles surface obtained through Karl Fischer Moisture Titrator. The surface water content of NCA-EPS was significantly less than that of NCA with decreasing to 1.28% from 2.77%, which indicates the formation of EPS coating could have a role to consume the trace H_2O on NCA particles surface.

Fig. 4a displays the charge and discharge profiles of NCA and NCA-EPS cathodes in the first cycle at 1/10 C with the voltage range of 2.8–4.3 V at 25 °C. NCA-EPS cathode exhibits the similar charge/discharge profile with NCA cathode, indicating that the additional redox reaction is not caused by covering EPS coating on NCA particles surface. NCA and NCA-EPS cathodes reveal the approximate initial discharge

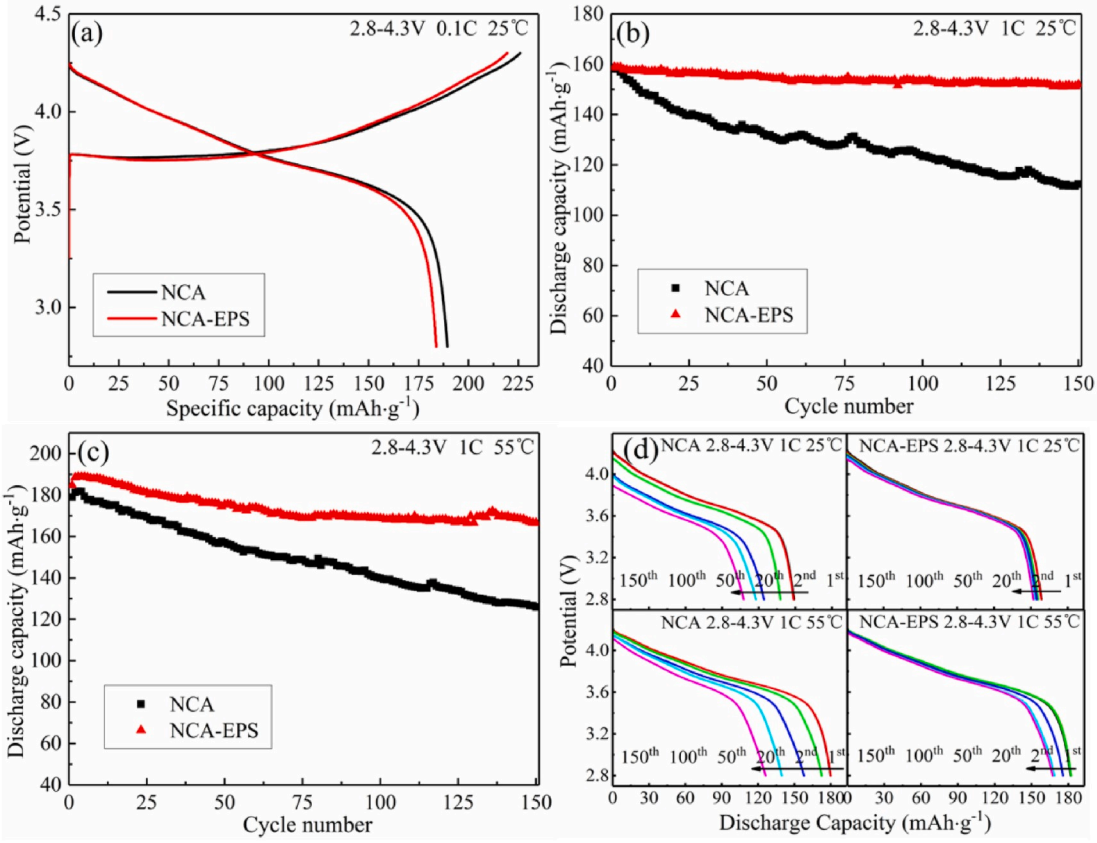

Fig. 4. (a) Initial charge-discharge curves of NCA and NCA-EPS at the current rate of 1/10 C; cycling performance of NCA and NCA-EPS at the current rate of 1C at 25 °C (b) and 55 °C (c); (d) the discharge voltage profile evolution of pristine NCA and NCA-EPS at 25 °C and 55 °C.

capacity and coulombic efficiencies, which are 189 and 184 mAh g^{-1} and 83.1 and 83.8%, respectively. The irreversible capacity loss origin usually from the formation of the surface phases because of the spinel-like defect structures triggered by oxygen loss [34]. The evolution from the layered to spinel/salt structure for NCA cathode derives from the decomposition of electrolyte and side reactions [57,58]. EPS coated on NCA particles surface could inhibit the interface reaction between the NCA particles and electrolyte, thus reducing the amount of irreversible Li^+ consumed during the formation of SEI film [59], which results in the decrease of the irreversible capacity loss for NCA-EPS cathode. However, as non-conductive EPS coated the surface of NCA particles, the interface resistance was increased to a certain extent, thus inhibiting the diffusion of lithium ions [60]. Therefore, EPS coating did not contribute to the improvement of coulombic efficiencies.

Fig. 4b and c depicts the cycling performance of NCA and NCA-EPS cathodes for 150 cycles at 1 C with the voltage range of 2.8–4.3 V at 25 and 55 °C. It is observed that the discharge capacity of NCA cathode declines obviously with the incremental cycle number, whereas slight reduction for NCA-EPS cathode. At 25 °C the discharge capacity still keeps ~96% of the original discharge capacity for NCA-EPS cathode after 150 cycles, whereas only ~70% residual rate of the original discharge capacity for NCA cathode. NCA-EPS cathode exhibits outstanding cyclic stability. At 55 °C, the cycle stability of NCA-EPS cathode is also significantly better than that of NCA cathode. Meantime, the original discharge capacities of samples are 179 and 185 mAh g^{-1}, which are larger than those of the both cathodes (158 and 159 mAh g^{-1}) at 25 °C. Because the diffusion coefficient of Li^+ is directly proportional to the temperature [61,62], high temperature will accelerate the diffusion speed of Li^+ and facilitate the intercalation/de-intercalation of Li^+, making the discharge capacity at 55 °C higher than that one at 25 °C. After 150 cycles, the capacity retention (~86%) of NCA-EPS cathode is higher than NCA cathode (~58%). In order to testify further the function of EPS coating, the cyclic performance data of NCA-EPS1 and NCA-EPS5 cathodes obtained by changing the TEOS content are display in Fig. S4, Table S1 and Table S2 (Supporting Information). It is found that the discharge capacities of NCA-EPS1 and NCA-EPS5 cathodes decrease gradually with the incremental cycle number. Meantime, the capacity retentions of the both cathodes at 1 C are lower than that one of NCA-EPS electrode after 150 cycles at 25 and 55 °C, respectively, but higher than those of NCA electrode. The results above indicate that the surface EPS coating can improve prominently the cycle stability of NCA electrode at low and high temperature. Additionally, the cyclic stability enhances first and then declines with the incremental TEOS level and attains the maximum as the mole ratios of TEOS to NCA is 0.03. The result suggests that the excellent cyclic stability results from the appropriate thickness of EPS coating with poor electrical conductivity on the surface of NCA particles.

The thermal stability of NCA and NCA-EPS as cathode materials could be further investigated by DSC analysis. DSC curves of NCA and NCA-EPS electrodes under the charged state of 4.3 V from room temperature to 400 °C are depict in Fig. S5 (Supporting Information). The exothermic reaction of the NCA electrode occurs approximately at 236.6 °C, whereas the exothermic peak shifts to higher temperature 260.1 °C for NCA-EPS electrode. Meantime, the exothermic peak area of the pristine NCA electrode is larger than that one of the NCA-EPS electrode. These result indicate that the thermal stability of the NCA cathode material could be enhanced via the aid of the EPS coating, which can suppress the interface reaction between the electrode and electrolyte and stabilize the interface. Generally, the use of insulator as coating can improve the cyclic stability of cathode materials, but it is also likely to limit the migration of Li^+ in the charging and discharging process [40]. Fortunately, during the formation of EPS coating, not only did H_2O on NCA surface be removed, but ethoxy-functional groups on polysiloxane could also react with harmful HF. In this way, the erosion rate of NCA particles and the formation of SEI are suppressed resulting in a stable cycling of NCA. Fig. 4d depicts the discharge capacity of NCA and NCA-EPS with different cycles at 25 °C and 55 °C. The voltage platform (Fig. S6, Supporting Information) of NCA has a faster voltage decay than NCA-EPS with the increase of cycles, indicating that the voltage degradation can be overcome with reasonable surface coating because the inhibition of the side reaction. More significantly, the capacity retention of NCA-ESP is higher than the values in recent reports of the other coating materials, such as, FeF_3 [26], $Ni_3(PO_4)_2$ [27], SnO_2 [63], MnO_2 [64], AlF_3 [24], $LiTiO_2$ [65], as indicated in Fig. S7 (Supporting Information).

Fig. 5 depicts the schematic diagram of the cycle performance of NCA cathode improved by EPS coating in Li-ion battery. The trace water on NCA surface could react with $LiPF_6$ to generate the harmful HF and by-products. And these by-products then react with residual Li on NCA surface to cover a non-conductive passivation layer, according to the following equation:

$$LiPF_6 + H_2O \rightarrow LiF\downarrow + POF_3 + HF \quad (5)$$

$$POF_3 + Li_2O/LiOH \rightarrow LiF \downarrow + Li_xPOF_y \quad (6)$$

In the long-term circulation process of NCA cathode, HF will continue to corrode the particles surface, and will cause the particles to crack or even break. The electrolyte then seeps into the primary particles of the cathode material, causing permanent damage to the material. Meantime, LiF could hinder the Li^+ ions diffusion, which result in the degenerative cycle performance of NCA. According to Karl Fischer Moisture Titrator analysis, the moisture on NCA particles surface is reduced obviously by covering the EPS coating, which suppresses the generation of corrosive HF and by-products. EPS skin protection can prevent the electrolyte from penetrating into the primary particles of the cathode to trigger the formation of miro-cracks and pulverization. In the case of the decrease of HF and by-products, the surface of NCA is improved and the Li^+ diffusion channel is augmented, which enhance significantly the cycle performance of NCA-EPS.

Fig. 6a and b shows the CV curves of the first three cycles for NCA and NCA-EPS cathodes. The profiles of CV curves change scarcely for the both cathodes, indicating that no additional redox reaction is introduced into the NCA cathode after coating EPS film. The main oxidation peaks of the NCA and NCA-EPS cathodes appear in the high potential of 3.94 and 3.92 V in the first cycle, whereas these peaks shift to the low potential of 3.84 and 3.74 V in the second cycle, which is caused by the first irreversible capacity loss. However, the reduction peaks for NCA and NCA-EPS cathodes do not shift in the first two cycles, manifesting that the first irreversible capacity loss is caused by the generation of SEI film [34,57,58]. SEI film could cause the partial Li^+ loss, resulting in the augment of surface polarization and the irreversible capacity loss. In addition, the reversibility of the electrochemical reaction can be estimated according to the potential difference (ΔE) of the redox peak. The smaller ΔE value means the better reversibility of the reaction [66,67]. As shown in Fig. 6a, in the second cycle the redox peaks of NCA cathode appear in the voltage of 3.84/3.68, 4.07/3.95 and 4.25/4.15 V, which are corresponding to the phase transitions of the hexagonal phase structure (H1)/monoclinal structure (M), M and the second hexagonal phase structure (H2) and H2 and the third hexagon phase structure (H3) [68]. The redox voltage difference ΔE values are 0.16, 0.12 and 0.10 V. However, the oxidation peaks of NCA-EPS cathode drift to low voltage and the reduction peaks to high voltage according to Fig. 6b. The redox peaks of H1/M, M/H2 and H2/H3 transformation locate at 3.74/3.70, 3.99/3.96 and 4.22/4.16 V, respectively. The ΔE values decrease to 0.04, 0.03 and 0.06 V compared to NCA cathode. The smaller ΔE values of NCA-EPS cathode suggest the improved reversibility of redox reaction and the decreased electrode polarization, which generate the excellent electrochemical stability for NCA-EPS cathode.

To study the effect of EPS coating on the NCA structural stability, the EIS test was conducted for the batteries uncirculated and after 150 cycles, as displayed in Fig. 6c. The insert is the equivalent circuit simulated by the Z-View software. Nyquist plots are usually consisted of two

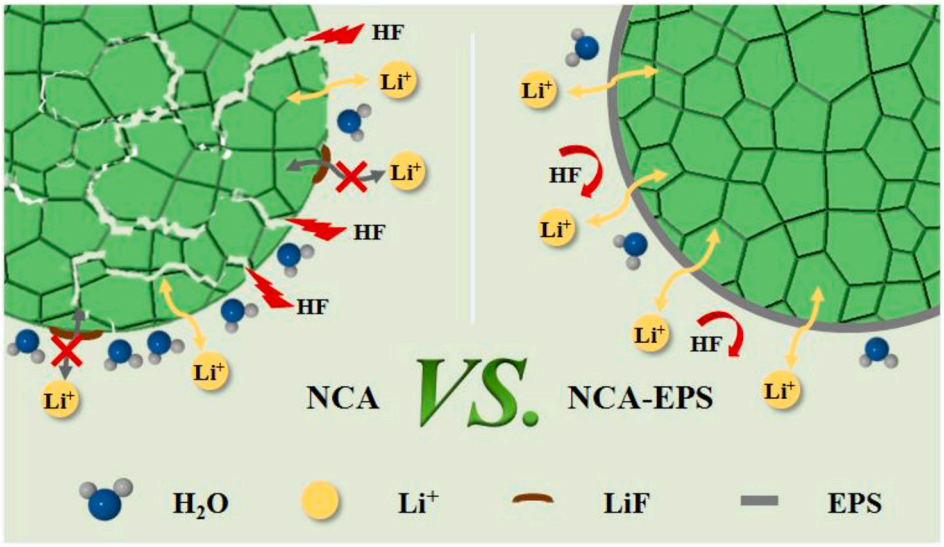

Fig. 5. The schematic diagram of the cycle performance of NCA cathode improved by EPS coating in Li-ion battery.

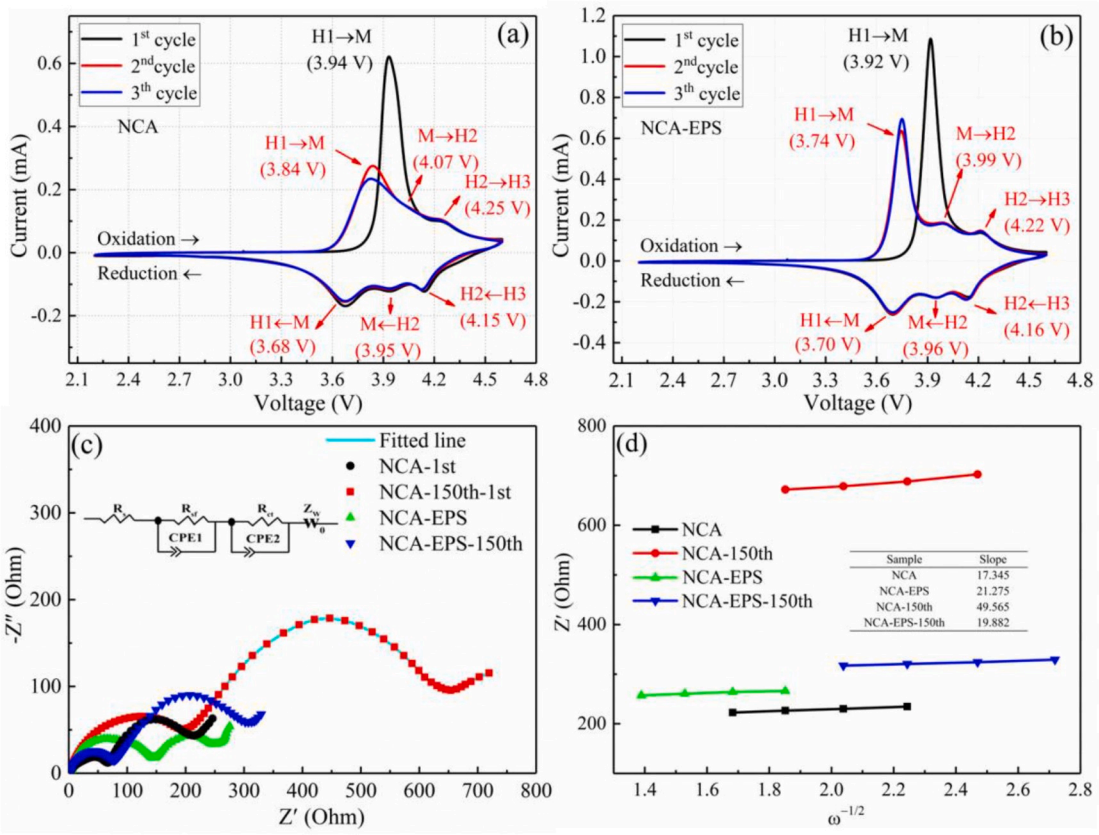

Fig. 6. Cyclic voltammetry curves of NCA (a) and NCA-EPS (b) at a scan rate of 0.1 mV s^{-1}; (c) Nyquist plots of NCA and NCA-EPS cathodes uncirculated and after 150 cycles in the voltage range of 2.7–4.3 V (vs. Li/Li^+), the insert is the equivalent circuit; (d) relationship between Z′ and $\omega^{-1/2}$ of NCA and NCA-EPS cathodes.

Table 2
The fitting resistance values and calculated values of D_{Li}^+ of NCA and NCA-EPS cathodes.

Sample	uncirculated			150th cycle		
	R_s	R_{ct}	$D_{Li}^+(cm^2\ s^{-1})$	R_s	R_{ct}	$D_{Li}^+(cm^2\ s^{-1})$
NCA	1.5	102.2	3.49×10^{-11}	2.1	467.3	4.27×10^{-12}
NCA-EPS	2.7	117.6	2.32×10^{-11}	2.4	247	2.65×10^{-11}

semicircles in middle and high frequencies and a line in low frequency. Herein, R_s is the system resistance, R_{ct} is the charge-transfer resistance and Z_w is the Warburg impedance [69]. The equivalent resistance R_s and R_{ct} values of NCA and NCA-EPS cathodes are presented in Table 2. The initial R_s (2.7 Ω) and R_{ct} (117.6 Ω) values of NCA-EPS cathode is larger than those of NCA cathode (1.5 and 102.2 Ω), which may be caused by the poor conductivity of the EPS coating. The R_s value of NCA cathode increases slightly to 2.1 Ω, whereas NCA-EPS cathode decreases to 2.4 Ω after 150 cycles. Meantime, the R_{ct} value of NCA cathode enhances

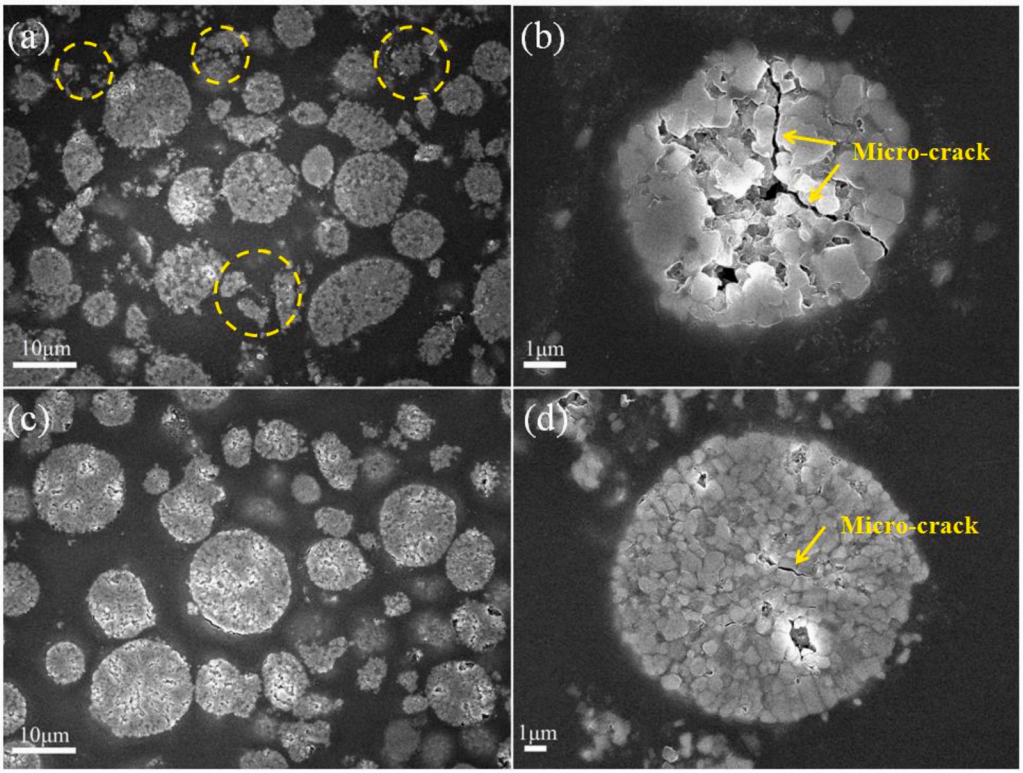

Fig. 7. The cross-sectional FESEM photos of NCA and NCA-EPS cathodes after 150 cycles: (a) NCA cathode at low magnification; (b) NCA cathode at high magnification; (c) NCA-EPS cathode at low magnification; (d) NCA-EPS cathode at high magnification.

significantly to 467.3 Ω from 102.2 Ω, whereas NCA–EPS cathode only augments to 247 Ω. The smaller R_s and R_{ct} values of NCA-EPS cathode after 150 cycles also verify the better electrochemical performance of NCA-EPS cathode.

The diffusion behavior of Li^+ was characterized by the diffusion coefficient of Li^+ in the cyclic process, which was calculated by the following formula [61,62]:

$$D_{Li^+} = R^2T^2/2A^2n^4F^4C^4\sigma^2 \quad (7)$$

where R is the gas constant, T is the absolute temperature, F is the Faraday constant, A is the area of the electrode plate (1.766×10^{-4} m^2), n is the number of transferred electrons (n = 2), C is the molar concentration of Li^+ (2.6×10^4 mol m^{-3}), and σ is the Warburg coefficient which was calculated from the following formula [49]:

$$Z' = R_s + R_{ct} + \sigma\omega^{-1/2} \quad (8)$$

According to Eq. (7), the D_{Li}^+ of NCA and NCA-EPS cathodes uncirculated and after 150 cycles were calculated and shown in Table 2. In the uncirculated samples, the D_{Li}^+ of NCA and NCA-EPS cathodes are 3.49×10^{-11} and 2.32×10^{-11} cm^2 s^{-1}, respectively. However, after 150 cycles the D_{Li}^+ of NCA cathode reduces about one order of magnitude to 4.27×10^{-12} cm^2 s^{-1} and D_{Li}^+ increases slightly to 2.65×10^{-11} cm^2 s^{-1} for NCA-EPS cathode. The side reaction between NCA particles surface and electrolyte would be reduced through the coating EPS film and the Li^+ diffusion is influenced scarcely during the 150 charge/discharge cycles, which result in the approximate diffusion coefficient D_{Li}^+ for NCA-EPS cathode. Inversely, NCA cathode reveals the lower diffusion coefficient than that of NCA-EPS cathode through the 150 cycle. In summary, the appropriate EPS film covered on the NCA particles surface can efficiently inhibit side reaction and lower the interface impedance of Li^+ diffusion, leading to the improved the cycle stability of NCA cathode.

To explore the mechanism of capacity loss and the difference in

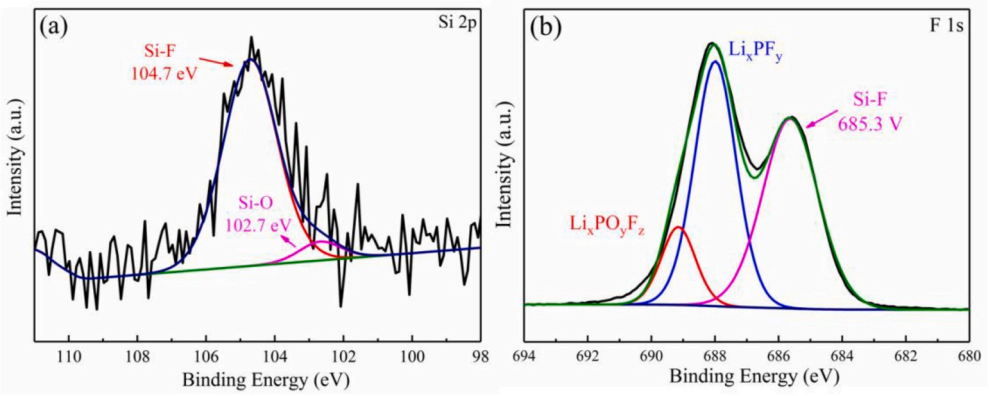

Fig. 8. The high resolution XPS spectra of Si 2p (a) and F 1s (b) of NCA-EPS cathode after 150 cycles.

electrochemical properties, the cathode materials was characterized after 150 cycles in the voltage range of 2.7–4.3 V (vs. Li/Li^+). Fig. 7a and d are the cross-section photos of NCA and NCA-EPS cathodes after 150 cycles at different magnification. The internal structural characteristics of the two particles were significantly different. The NCA particles from Fig. 7a are subjected to destruction after 150 cycles. At high magnification (Fig. 7b) it is found that the aggregation of grains emerges dramatically the micro-cracks and a part of grains are desquamated from the surface of aggregation. As the number of cycles increases, the individual particles may split completely. Intergranular cracks have been identified as one factors for the degradation of the cathode material and its failure during the cycles [70]. The surface and internal structure of NCA particles generate the difference owning to the HF corrosion. The micro-cracks and exfoliated grains would be generated by the strain derived from expansion and contraction of the different structure during the consecutive charge/discharge cycles. The micro-cracks allow electrolyte to penetrate into the interior of particles to form SEI film and NiO-like interface layer with the incremental cycle number [71,72], which lead to a reduced electrical contact between the particles and inhibit the release of Li^+. The contribution of the isolated particles to capacity would decrease [73], which results in the decaying cycle performance of NCA cathode. However, the NCA particles coated by EPS still remain in an intact state at the same cycle number in Fig. 7c. Also from Fig. 7d, the micro-crack and exfoliated grains are alleviated prominently on the aggregation surface, which enhances the cycle performance of NCA cathode.

Fig. 8a and b reveal the high resolution XPS spectra of Si 2p and F 1s of NCA-EPS cathode after 100 cycles. For Si 2p spectrum it is observed that a main peak and a weak peak appear at 104.7 and 102.7 eV, respectively. The former represents the Si–F bond that is generated through a nucleophilic reaction site provided by the ethoxy-functional group between Si and F. The reaction equation may be expressed as follows [39]:

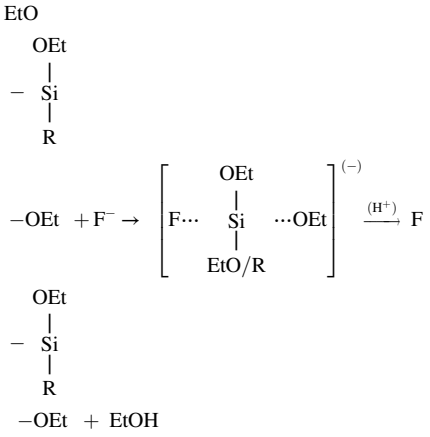

(9)

And the latter is assigned to Si–O bond from EPS. As for F 1s spectra, the peak at 685.3 eV is corresponding to Si–F bond [74,75]. The peaks at 688 and 689.2 eV are associated with Li_xPF_y [76] and $Li_xPO_yF_z$ [77]. The above results show that EPS film could capture F^- species to form Si–F bond during the charge/discharge cycle, removing harmful HF and enhances the surface stability of NCA particles, which lead to the improved cycle performance of NCA-EPS cathode.

4. Conclusions

EPS film as a protective layer was successfully grown on NCA particles surface through the TEOS hydrolysis-condensation method without heating treatment. Results indicate that NCA-EPS cathode has excellent cycle performance at room temperature (25 °C) and high temperature (55 °C). These improvements are attributed to TEOS hydrolysis consumed trace H_2O on NCA particles surface in the synthesis process, thereby reducing the generation of harmful substance HF. Additionally, HF can be further cleared by polysiloxane with ethoxy-functional groups produced by TEOS hydrolysis. The original discharge capacities of NCA and NCA-EPS cathodes are 158.2 and 158.9 $mAh{\cdot}g^{-1}$ at 25 °C, respectively. After 150 cycles the capacity retention of NCA-EPS cathode is ~96% of the original discharge capacity, which is 25% higher than that of NCA cathode. Even at high temperatures of 55 °C, NCA-EPS cathode could maintain ~86% of the original discharge capacity through 150 cycles, which enhances 29% compared to NCA cathode. EPS coating plays a crucial role in the barrier to suppress the penetration of the electrolyte into the secondary particles to alleviate the interfacial side reactions, and scavenge HF to eliminate the side reactions, providing an effective approach to obtain the stable NCA cathode for high energy density batteries.

Declaration of competing interest

The authors declare that they have no known competing financial interests or personal relationships that could have appeared to influence the work reported in this paper.

CRediT authorship contribution statement

Zi Yang: Conceptualization, Methodology, Software, Investigation, Writing - original draft. **Zhimin Li:** Resources, Writing - review & editing, Supervision, Data curation. **Yunxia Huang:** Validation, Formal analysis, Software, Writing - review & editing. **Maolin Zhang:** Writing - review & editing. **Chaofeng Liu:** Writing - review & editing. **Dongyan Zhang:** Formal analysis, Software. **Guozhong Cao:** Resources, Writing - review & editing, Supervision, Data curation.

Acknowledgements

This work was supported partly by the National Natural Science Foundation of China (No. 61974114).

Appendix A. Supplementary data

Supplementary data to this article can be found online at https://doi.org/10.1016/j.jpowsour.2020.228480.

References

[1] Z.G. Yang, J.L. Zhang, M.C.W. Kintner-Meyer, X.C. Lu, D.W. Choi, J.P. Lemmon, J. Liu, Electrochemical energy storage for green grid, Chem. Rev. 111 (5) (2011) 3577–3613.
[2] C.F. Liu, J.F. Yuan, R. Masse, X.X. Jia, W.C. Bi, Z. Neale, T. Shen, M. Xu, M. Tian, J. Q. Zheng, J.J. Tian, G.Z. Cao, Interphases, interfaces, and surfaces of active materials in rechargeable batteries and perovskite solar cells, Adv. Mater. (2020), https://doi.org/10.1002/adma.201905245.
[3] M.M. Thackeray, C. Wolverton, E.D. Isaacs, Electrical energy storage for transportation-approaching the limits of, and going beyond, lithium-ion batteries, Energy Environ. Sci. 5 (7) (2012) 7854.
[4] E. Pomerantseva, F. Bonaccorso, X.L. Feng, Y. Cui, Y. Gogotsi, Energy storage: the future enabled by nanomaterials, Science 366 (2019) 6468.
[5] J.C. Zheng, Z. Yang, A. Dai, L.B. Tang, H.X. Wei, Y.J. Li, Z.J. He, J. Lu, Boosting cell performance of $LiNi_{0.8}Co_{0.15}Al_{0.05}O_2$ via surface structure design, Small 15 (50) (2019) 1904854.
[6] J.C. Chen, L. Zhu, D. Jia, X.X. Jiang, Y.M. Wu, Q.L. Hao, X.F. Xia, Y. Ouyang, L. M. Peng, W.P. Tang, T. Liu, $LiNi_{0.8}Co_{0.15}Al_{0.05}O_2$ cathodes exhibiting improved capacity retention and thermal stability due to a lithium iron phosphate coating, Electrochim. Acta 312 (2019) 179–187.
[7] Z.Y. Luo, H. Zhang, L. Yu, D.H. Huang, J.Q. Shen, Improving long-term cyclic performance of $LiNi_{0.8}Co_{0.15}Al_{0.05}O_2$ cathode by introducing a film forming additive, J. Electroanal. Chem. 833 (2019) 520–526.
[8] L. Qiu, W. Xiang, W. Tian, C.L. Xu, Y.C. Wu, T.R. Chen, K. Jia, D. Wang, F.R. He, X. D. Guo, Polyanion and cation co-doping stabilized Ni-rich Ni-Co-Al material as cathode with enhanced electrochemical performance for Li-ion battery, Nano Energy 63 (2019) 103818.
[9] L.W. L, W.H. Z, F. Z, D.K. Denis, F. Zaman, L.R. H, C.Z. Y, Surface/interface structure degradation of Ni-rich layered oxide cathodes toward lithium-ion batteries: fundamental mechanisms and remedying strategies, Adv. Mater. Interf. 7 (2020) 3.

[10] S. Watanabe, M. Kinoshita, K. Nakura, Capacity fade of $LiNi_{(1-x-y)}Co_xAl_yO_2$ cathode for lithium-ion batteries during accelerated calendar and cycle life test. I. Comparison analysis between $LiNi_{(1-x-y)}Co_xAl_yO_2$ and $LiCoO_2$ cathodes in cylindrical lithium-ion cells during long term storage test, J. Power Sources 247 (2014) 412–422.

[11] N.V. Faenza, Z.W. Lebens-Higgins, P. Mukherjee, S. Sallis, N. Pereira, F. Badway, A. Halaijko, G. Ceder, F. Cosandey, L.F.J. Piper, G.G. Amatucci, Electrolyte-induced surface transformation and transition-metal dissolution of fully delithiated $LiNi_{0.8}Co_{0.15}Al_{0.05}O_2$, Langmuir 33 (37) (2017) 9333–9353.

[12] S. Muto, Y. Sasano, K. Tatsumi, T. Sasaki, K. Horibuchi, Y. Takeuchi, Y. Ukyo, Capacity-fading mechanisms of $LiNiO_2$-based lithium-ion batteries II. Diagnostic analysis by electron microscopy and spectroscopy, J. Electrochem. Soc. 156 (5) (2009) A371–A377.

[13] W. Liu, P. Oh, X.E. Liu, M.J. Lee, W. Cho, S. Chae, Y. Kim, J. Cho, Nickel-rich layered lithium transition-metal oxide for high-energy lithium-ion batteries, Angew. Chem. Int. Ed. 54 (15) (2015) 4440–4457.

[14] M.D. Radin, S. Hy, M. Sina, C.C. Fang, H.D. Liu, J. Vinckeviciute, M.H. Zhang, M. S. Whittingham, Y.S. Meng, A.V.der Ven, Narrowing the gap between theoretical and practical capacities in Li-ion layered oxide cathode materials, Advanced Energy Materials 7 (20) (2017) 1602888.

[15] P.F. Yan, J.M. Zheng, J.G. Zhang, C.M. Wang, Atomic resolution structural and chemical imaging revealing the sequential migration of Ni, Co, and Mn upon the battery cycling of layered cathode, Nano Lett. 17 (6) (2017) 3946–3951.

[16] A. Grenier, H. Liu, K.M. Wiaderek, Z.W. Lebens-Higgins, O.J. Borkiewicz, L.F. J. Piper, P.J. Chupas, K.W. Chapman, Reaction heterogeneity in $LiNi_{0.8}Co_{0.15}Al_{0.05}O_2$ induced by surface layer, Chem. Mater. 29 (17) (2017) 7345–7352.

[17] T. Yim, K.S. Kang, J. Mun, S.H. Lim, S.G. Woo, K.J. Kim, M.S. Park, W. Cho, J. H. Song, Y.K. Han, J.S. Yu, Y.J. Kim, Understanding the effects of a multi-functionalized additive on the cathode-electrolyte interfacial stability of Ni-rich materials, J. Power Sources 302 (2016) 431–438.

[18] X.X. Yan, L. Chen, S.A. Shahb, J.J. Liang, Z.F. Liu, The effect of Co_3O_4 & $LiCoO_2$ cladding layer on the high rate and storage property of high nickel material $LiNi_{0.8}Co_{0.15}Al_{0.05}O_2$ by simple one-step wet coating method, Electrochim. Acta 249 (2017) 179–188.

[19] L.W. L, X. S, C. W, L.R. H, J.F. S, X.G. Z, C.Z. Y, Nasicon-type surface functional modification in core-shell $LiNi_{0.5}Mn_{0.3}Co_{0.2}O_2$@$NaTi_2(PO_4)_3$ cathode enhances its high-voltage cycling stability and rate capacity toward Li-ion batteries, ACS Appl. Mater. Interfaces 10 (6) (2018) 5498–5510.

[20] P.F. Zhou, Z. Zhang, H.J. Meng, Y.Y. Lu, J. Cao, F.Y. Cheng, Z.L. Tao, J. Chen, SiO_2 coated $LiNi_{0.915}Co_{0.075}Al_{0.01}O_2$ cathode material for rechargeable Li-ion batteries, Nanoscale 8 (46) (2016) 19263–19269.

[21] W.K. Shin, J.H. Yoo, W. Choi, K.Y. Chung, S.S. Jangc, D.W. Kim, Cycling performance of lithium-ion polymer cells assembled with a cross-linked composite polymer electrolyte using a fibrous polyacrylonitrile membrane and vinyl-functionalized SiO_2 nanoparticles, J. Mater. Chem. 3 (23) (2015) 12163–12170.

[22] Y. Xu, X.H. Li, Z.X. Wang, H.J. Guo, B. Huang, Structure and electrochemical performance of TiO_2-coated $LiNi_{0.80}Co_{0.15}Al_{0.05}O_2$ cathode material, Mater. Lett. 143 (2015) 151–154.

[23] K. Du, H.H. Xie, G.R. Hu, Z.D. Peng, Y.B. Cao, F. Yu, Enhancing the thermal and upper voltage performance of Ni-Rich cathode material by a homogeneous and facile coating method: spray-drying coating with nano-Al_2O_3, ACS Appl. Mater. Interfaces 8 (27) (2016) 17713–17720.

[24] S.H. Lee, C.S. Yoon, K. Amine, Y.K. Sun, Improvement of long-term cycling performance of $Li[Ni_{0.8}Co_{0.15}Al_{0.05}]O_2$ by AlF_3 coating, J. Power Sources 234 (2013) 201–207.

[25] B.C. Park, H.B. Kim, H.J. Bang, J. Prakash, Y.K. Sun, Improvement of electrochemical performance of $Li[Ni_{0.8}Co_{0.15}Al_{0.05}]O_2$ cathode materials by AlF_3 coating at various temperatures, Ind. Eng. Chem. Res. 47 (11) (2008) 3876–3882.

[26] W. Liu, X. Tang, M.L. Qin, G.L. Li, J.Y. Deng, X.W. Huang, FeF_3-coated $LiNi_{0.8}Co_{0.15}Al_{0.05}O_2$ cathode materials with improved electrochemical properties, Mater. Lett. 185 (2016) 96–99.

[27] D.J. Lee, B. Scrosati, Y.K. Sun, $Ni_3(PO_4)_2$-coated $Li[Ni_{0.8}Co_{0.15}Al_{0.05}]O_2$ lithium battery electrode with improved cycling performance at 55 °C, J. Power Sources 196 (18) (2011) 7742–7746.

[28] B. Huang, X.H. Li, Z.X. Wang, H.J. Guo, A facile process for coating amorphous $FePO_4$ onto $LiNi_{0.8}Co_{0.15}Al_{0.05}O_2$ and the effects on its electrochemical properties, Mater. Lett. 131 (2014) 210–213.

[29] P.F. Yan, J.M. Zheng, J. Liu, B.Q. Wang, X.P. Chen, Y.F. Zhang, X.L. Sun, C. M. Wang, J.G. Zhang, Tailoring grain boundary structures and chemistry of Ni-rich layered cathodes for enhanced cycle stability of lithium-ion batteries, Nature Energy 3 (7) (2018) 600–605.

[30] S. Ito, S. Fujiki, T. Yamada, Y. Aihara, Y. Park, T.Y. Kim, S.W. Baek, J.M. Lee, S. Doo, N. Machida, A rocking chair type all-solid-state lithium ion battery adopting Li_2O-ZrO_2 coated $LiNi_{0.8}Co_{0.15}Al_{0.05}O_2$ and a sulfide based electrolyte, J. Power Sources 248 (2014) 943–950.

[31] S.N. Lima, W. Ahnb, S.H. Yeonb, S.B. Parka, Enhanced elevated-temperature performance of $Li(Ni_{0.8}Co_{0.15}Al_{0.05})O_2$ electrodes coated with Li_2O-$2B_2O_3$ glass, Electrochim. Acta 136 (2014) 1–9.

[32] S. Yoon, K.N. Jung, S.H. Yeon, C.S. Jin, K.H. Shin, Electrochemical properties of $LiNi_{0.8}Co_{0.15}Al_{0.05}O_2$-graphene composite as cathode materials for lithium-ion batteries, J. Electroanal. Chem. 683 (2012) 88–93.

[33] L.P. Zhang, J. Fu, C.H. Zhang, Mechanical composite of $LiNi_{0.8}Co_{0.15}Al_{0.05}O_2$/Carbon nanotubes with enhanced electrochemical performance for lithium-ion batteries, Nanoscale Research Letters 12 (1) (2017) 376.

[34] G.L. Xu, Q. Liu, K.K.S. Lau, Y.Z. Liu, X. Liu, H. Gao, X.W. Zhou, M.H. Zhuang, Y. Ren, J.D. Li, M.H. Shao, M.G. Ouyang, F. Pan, Z.H. Chen, K. Amine, G.H. Chen, Building ultraconformal protective layers on both secondary and primary particles of layered lithium transition metal oxide cathodes, Nature Energy 4 (6) (2019) 484–494.

[35] H. Visbal, S. Fujiki, Y. Aihara, T. Watanabe, Y. Park, S. Doo, The influence of the carbonate species on $LiNi_{0.8}Co_{0.15}Al_{0.05}O_2$ surfaces for all-solid-state lithium ion battery performance, J. Power Sources 269 (2014) 396–402.

[36] J. Kim, H. Ma, H. Cha, H. Lee, J. Sung, M. Seo, P. Oh, M. Park, J. Cho, A highly stabilized nickel-rich cathode material by nanoscale epitaxy control for high-energy lithium-ion batteries, Energy Environ. Sci. 11 (6) (2018) 1449–1459.

[37] J. Kim, J. Lee, H. Ma, H.Y. Jeong, H. Cha, H. Lee, Y. Yoo, M. Park, J. Cho, Controllable solid electrolyte interphase in nickel-rich cathodes by an electrochemical rearrangement for stable lithium-ion batteries, Adv. Mater. 30 (5) (2018), 1704309.

[38] H.T. Pu, F.J. Jiang, Z.L. Yang, Studies on preparation and chemical stability of reduced iron particles encapsulated with polysiloxane nano-films, Mater. Lett. 60 (1) (2006) 94–97.

[39] H.J. Naghash, R. Mohammadrahimpanah, Synthesis and characterization of new polysiloxane bearing vinylic function and its application for the preparation of poly (silicone-co-acrylate)/montmorillonite nanocomposite emulsion, Prog. Org. Coating 70 (1) (2011) 32–38.

[40] F. Abbasi, H. Mirzadeh, A.A. Katbab, Modification of polysiloxane polymers for biomedical applications: a review, Polym. Int. 50 (12) (2001) 1279–1287.

[41] E.J.A. Pope, J.D. Mackenzie, Sol-gel processing of silica: II. The role of the catalyst, J. Non-Cryst. Solids 87 (1–2) (1986) 185–198.

[42] H. Wang, W.J. Ge, W. Li, F. Wang, W.J. Liu, M.Z. Qu, G.C. Peng, Facile fabrication of ethoxy-functional polysiloxane wrapped $LiNi_{0.6}Co_{0.2}Mn_{0.2}O_2$ cathode with improved cycling performance for rechargeable Li-ion battery, ACS Appl. Mater. Interfaces 8 (28) (2016) 18439–18449.

[43] W. Li, M.Z. Chen, J.J. Jiang, R. Wu, F. Wang, W.J. Liu, G.C. Peng, M.Z. Qu, Structural and electrochemical characteristics of SiO_2 modified $Li_4Ti_5O_{12}$ as anode for lithium-ion batteries, J. Alloys Compd. 637 (2015) 476–482.

[44] Z. Wang, Y.D. Huang, X.C. Wang, D.Z. Jia, Z.P. Guo, M. Miao, Tetraethoxysilane as a new facilitative film-forming additive for the lithium-ion battery with $LiMn_2O_4$ cathode, Solid State Ionics 232 (2013) 19–23.

[45] Y.C. Li, W. Xiang, Z.G. Wu, C.L. Xu, Y.D. Xu, Y. Xiao, Z.G. Yang, C.J. Wu, G.P. Lv, X. D. Guo, Construction of homogeneously Al^{3+} doped Ni rich Ni-Co-Mn cathode with high stable cycling performance and storage stability via scalable continuous precipitation, Electrochim. Acta 291 (2018) 84–94.

[46] X.F. Luo, X.Y. Wang, L. Liao, S. Gamboab, P.J. Sebastian, Synthesis and characterization of high tap-density layered $Li[Ni_{1/3}Co_{1/3}Mn_{1/3}]O_2$ cathode material via hydroxide co-precipitation, J. Power Sources 158 (1) (2006) 654–658.

[47] Z.G. Wang, Z.X. Wang, H.J. Guo, W.J. Peng, X.H. Li, Improving the cycling stability of $LiCoO_2$ at 4.5 V through co-modification by Mg doping and zirconium oxyfluoride coating, Ceram. Int. 41 (1) (2015) 469–474.

[48] D.C. Li, T. Muta, L.Q. Zhang, M. Yoshio, H. Noguchi, Effect of synthesis method on the electrochemical performance of $LiNi_{1/3}Mn_{1/3}Co_{1/3}O_2$, J. Power Sources 132 (1–2) (2004) 150–155.

[49] Y.C. Li, W. Xiang, Y. Xiao, Z.G. Wu, C.L. Xu, W. Xu, Y.D. Xu, C. Wu, Z.G. Yang, X. D. Guo, Synergy of doping and coating induced heterogeneous structure and concentration gradient in Ni-rich cathode for enhanced electrochemical performance, J. Power Sources 423 (2019) 144–151.

[50] B.S. Liu, Z.B. Wang, F.D. Yu, Y. Xue, G.J. Wang, Y. Zhang, Y.X. Zhou, Facile strategy of NCA cation mixing regulation and its effect on electrochemical performance, RSC Adv. 6 (2016) 110.

[51] W.S. Yoon, K.Y. Chung, J. McBreen, X.Q. Yang, A comparative study on structural changes of $LiCo_{1/3}Ni_{1/3}Mn_{1/3}O_2$ and $LiNi_{0.8}Co_{0.15}Al_{0.05}O_2$ during first charge using in situ XRD, Electrochem. Commun. 8 (8) (2006) 1257–1262.

[52] G.R. Hu, M.F. Zhang, L.W. Liang, Z.D. Peng, K. Du, Y.B. Cao, Mg-Al-B co-substitution $LiNi_{0.5}Co_{0.2}Mn_{0.3}O_2$ cathode materials with improved cycling performance for lithium-ion battery under high cutoff voltage, Electrochim. Acta 190 (2016) 264–275.

[53] X. Li, W.J. Ge, H. Wang, X.X. Yan, B.W. Deng, T. Chen, M.Z. Qu, Enhancing cycle stability and storage property of $LiNi_{0.8}Co_{0.15}Al_{0.05}O_2$ by using fast cooling method, Electrochim. Acta 227 (2017) 225–234.

[54] L. Zhu, Y. Liu, W.Y. Wu, X.W. Wu, W.P. Tang, Y.P. Wu, Surface fluorinated $LiNi_{0.8}Co_{0.15}Al_{0.05}O_2$ as a positive electrode material for lithium ion batteries, J. Mater. Chem. 3 (29) (2015) 15156–15162.

[55] N.V. Kosova, E.T. Devyatkina, V.V. Kaichev, Optimization of Ni^{2+}/Ni^{3+} ratio in layered Li(Ni, Mn, Co)O_2 cathodes for better electrochemistry, J. Power Sources 174 (2) (2007) 965–969.

[56] J. Zhang, Q.W. Lu, J.H. Fang, J.L. Wang, J. Yang, Y.N. Li, Polyimide encapsulated lithium-rich cathode material for high voltage lithium-ion battery, ACS Appl. Mater. Interfaces 6 (20) (2014) 17965–17973.

[57] Q. Wang, C.H. Shen, S.Y. Shen, Y.F. Xu, C.G. Shi, L. Huang, J.T. Li, S.G. Sun, Origin of structural evolution in capacity degradation for overcharged NMC622 via operando coupled investigation, ACS Appl. Mater. Interfaces 9 (29) (2017) 24731–24742.

[58] Y.M. Lee, K.M. Nam, E.H. Hwang, Y.G. Kwon, D.H. Kang, S.S. Kim, S.W. Song, Interfacial origin of performance improvement and fade for 4.6 V $LiNi_{0.5}Co_{0.2}Mn_{0.3}O_2$ battery cathodes, J. Phys. Chem. C 118 (20) (2014) 10631–10639.

[59] J.J. Chen, Z.D. Li, H.F. Xiang, W.W. Wu, S. Cheng, L.J. Zhang, Q.S. Wang, Y.C. Wu, Enhanced electrochemical performance and thermal stability of a $CePO_4$-coated

$Li_{1.2}Ni_{0.13}Co_{0.13}Mn_{0.54}O_2$ cathode material for lithium-ion batteries, RSC Adv. 5 (4) (2015) 3031–3038.
[60] Z.G. Wang, Z.X. Wang, H.J. Guo, W.J. Peng, X.H. Li, Synthesis of Li_2MnO_3-stabilized $LiCoO_2$ cathode material by spray-drying method and its high-voltage performance, J. Alloys Compd. 626 (2015) 228–233.
[61] Z.Q. Huo, Y.T. Cui, D. Wang, Y. Dong, L. Chen, The influence of temperature on a nutty-cake structural material: $LiMn_{1-x}Fe_xPO_4$ composite with $LiFePO_4$ core and carbon outer layer for lithium-ion battery, J. Power Sources 245 (2014) 331–336.
[62] L.J. Li, Z.Y. Chen, Q.B. Zhang, M. Xu, X. Zhou, H.L. Zhu, K.L. Zhang, A hydrolysis-hydrothermal route for the synthesis of ultrathin $LiAlO_2$-inlaid $LiNi_{0.5}Co_{0.2}Mn_{0.3}O_2$ as a high-performance cathode material for lithium ion batteries, J. Mater. Chem. 3 (2) (2015) 894–904.
[63] Z.C. Xie, Y.Y. Zhang, A.B. Yuan, J.Q. Xu, Effects of lithium excess and SnO_2 surface coating on the electrochemical performance of $LiNi_{0.8}Co_{0.15}Al_{0.05}O_2$ cathode material for Li-ion batteries, J. Alloys Compd. 787 (2019) 429–439.
[64] J.K. Zhao, Z.X. Wang, J.X. Wang, H.J. Guo, X.H. Li, G.C. Yan, W.H. Gui, N. Chen, The role of a MnO_2 functional layer on the surface of Ni-rich cathode materials: towards enhanced chemical stability on exposure to air, Ceram. Int. 44 (11) (2018) 13341–13348.
[65] P.C. Liu, L. Xiao, Y.F. Chen, H. Chen, Highly enhanced electrochemical performances of $LiNi_{0.815}Co_{0.15}Al_{0.035}O_2$ by coating via conductively $LiTiO_2$ for lithium-ion batteries, Ceram. Int. 45 (2019) 18398–18405.
[66] X.H. Xiong, Z.X. Wang, G.C. Yan, H.J. Guo, X.H. Li, Role of V_2O_5 coating on $LiNiO_2$-based materials for lithium ion battery, J. Power Sources 245 (2014) 183–193.
[67] B. Zhang, P.Y. Dong, H. Tong, Y.Y. Yao, J.C. Zheng, W.J. Yu, J.F. Zhang, D.W. Chu, Enhanced electrochemical performance of $LiNi_{0.8}Co_{0.1}Mn_{0.1}O_2$ with lithium-reactive Li_3VO_4 coating, J. Alloys Compd. 706 (2017) 198–204.
[68] H.J. Noh, S. Youn, C.S. Yoon, Y.K. Sun, Comparison of the structural and electrochemical properties of layered $Li[Ni_xCo_yMn_z]O_2$ (x= 1/3, 0.5, 0.6, 0.7, 0.8 and 0.85) cathode material for lithium-ion batteries, J. Power Sources 233 (2013) 121–130.
[69] S.S. Z, Identifying rate limitation and a guide to design of fast-charging Li-ion battery, Info (2019) 1–8.
[70] D.J. Miller, C. Proff, J.G. Wen, D.P. Abraham, J. Bareño, Observation of microstructural evolution in Li battery cathode oxide particles by in situ electron microscopy, Advanced Energy Materials 3 (8) (2013) 1098–1103.
[71] H. Kim, M.G. Kim, H.Y. Jeong, H. Nam, J. Cho, A new coating method for alleviating surface degradation of $LiNi_{0.6}Co_{0.2}Mn_{0.2}O_2$ cathode material: nanoscale surface treatment of primary particles, Nano Lett. 15 (3) (2015) 2111–2119.
[72] H. Liu, M. Wolf, K. Karki, Y.S. Yu, E.A. Stach, J. Cabana, K.W. Chapman, P. J. Chupas, Inter-granular cracking as a major cause of long-term capacity fading of layered cathodes, Nano Lett. 17 (6) (2017) 3452–3457.
[73] S. Watanabe, M. Kinoshita, T. Hosokawa, K. Morigaki, K. Nakura, Capacity fade of $LiAl_yNi_{1-x-y}Co_xO_2$ cathode for lithium-ion batteries during accelerated calendar and cycle life tests (surface analysis of $LiAl_yNi_{1-x-y}Co_xO_2$ cathode after cycle tests in restricted depth of discharge ranges), J. Power Sources 258 (2014) 210–217.
[74] V. Wheeler, N. Garces, L. Nyakiti, R. Myers-Ward, G. Jernigan, J. Culbertson, C. Eddy Jr., D.K. Gaskill, Fluorine functionalization of epitaxial graphene for uniform deposition of thin high-κ dielectrics, Carbon 50 (2012) 2307–2314.
[75] C.C. Nguyen, H. Choi, S.W. Song, Roles of oxygen and interfacial stabilization in enhancing the cycling ability of silicon oxide anodes for rechargeable lithium batteries, J. Electrochem. Soc. 160 (2013) A906–A914.
[76] D. Ensling, M. Stjerndahl, A. Nyten, T. Gustafsson, J.O. Thomas, A comparative XPS surface study of Li_2FeSiO_4/C cycled with LiTFSI-and $LiPF_6$-based electrolytes, J. Mater. Chem. 19 (2009) 82–88.
[77] W. Li, B.L. Lucht, Lithium-ion batteries: thermal reactions of electrolyte with the surface of metal oxide cathode particles, J. Electrochem. Soc. 153 (2006) A1617–A1625.